Oxygen Permeation of Various Archetypes of Oxygen Membranes Based on BSCF

Matthias Schulz, Ute Pippardt, Lutz Kiesel, Katrin Ritter, and Ralf Kriegel
Dept. of Environmental Engineering and Bioenergy, Fraunhofer Institute for Ceramic Technologies and Systems,
Michael Faraday Straße 1, Hermsdorf 07629, Germany

DOI 10.1002/aic.13843

$Ba_{0.5}Sr_{0.5}Co_{0.8}Fe_{0.2}O_{3-\delta}$ tubes, capillaries, capillary modules, and asymmetric membranes were prepared and tested for oxygen permeation in a dead-end vacuum operation mode at temperatures up to 850°C. The capillary module was built up by reactive air brazing using seven capillaries and a supply tube. Two machined discs were used as an end cap and as a connector plate. The oxygen permeation behaves according to Wagner at small driving forces, but significant negative deviations were observed for asymmetric membranes and single capillaries at higher ones. This is caused by pressure drops at the vacuum side for single capillaries. The highest oxygen flux was revealed for the capillary module with 175.5 mL(STP)/min at a low-vacuum pressure of 0.042 bar at 850°C, but the asymmetric membrane showing a little bit higher flux at moderate vacuum pressures above 0.07 bar. © 2012 American Institute of Chemical Engineers *AIChE J,* 58: 3195–3202, 2012
Keywords: oxygen membrane, mixed conductor, capillaries, asymmetric membrane

Introduction

Oxygen separation at high temperatures using mixed ionic electronic conductor (MIEC) membranes is an energy-efficient alternative to cryogenic air separation, especially if the high temperature of a combustion or a gasification process can be used. Nevertheless, a reliable economic comparison to mature technologies like cryogenic air separation is difficult for this preindustrial technology because of the lack of reliable data regarding the capital cost for membrane production, the uncertain lifetime of membrane components, the influence of operation conditions on the energy demand, on the reactor dimensions, and on the oxygen flux. Several authors propose the use of a minimal oxygen flux density of 10 mL(STP)/(cm^2 min) as a limit for competitive operation[1] or postulate a maximal gas speed of 25 m/s at the membrane surface[2] to compare different membrane components. Recently, it was shown that the production costs for a membrane area of 10,000 m^2 differs significantly for different membrane archetypes as well as the absolute oxygen production rate.[3] Capillary bunches were especially preferred compared to planar cell stacks and monolithic tubes because of the lower production costs, the high oxygen flux per volume and comparable low-mechanical tensile stress caused by outer loads and chemical expansion. In addition, this article deals with a detailed comparison of the oxygen flux of different archetypes of oxygen membranes based on $Ba_{0.5}Sr_{0.5}Co_{0.8}Fe_{0.2}O_{3-\delta}$ (BSCF). This material known for its high oxygen permeation[4–8] showing a phase decomposition at intermediate temperatures[9,10] but can be used for stable oxygen production at 850°C and above.[11]

Aside from inherent material properties there are different opportunities to enhance the oxygen permeation, for example, by enhancing the driving force or by lowering the membrane thickness resulting in the concept of asymmetric membranes. For a given separation process like oxygen production from air, the minimization of the reactor volume is also a promising way to decrease the capital costs and the energy demand by lowering the thermal losses. The driving force for oxygen production with MIEC membranes has to be realized by compression of feed air or by oxygen withdrawal with a vacuum pump or by a combination thereof. The production of pure oxygen does not need a sweep gas, and therefore, the gas management is more simple, especially, if a vacuum process without any overpressure at the feed side is used.

Regarding the energy demand of oxygen production, it has to be kept in mind that the whole driving force has to be realized by compression of air or extraction of oxygen by vacuum. The energy demand for gas compression amounts only a fifth for the latter one because of the lower gas volume of permeated oxygen compared to feed air. In addition, vacuum process using feed air at environmental pressure needs only one gas-tight oxygen supply and no external pressure vessel as the membrane itself serves as a pressure shell. Moreover, the oxygen permeation is higher for vacuum operation compared to sweep gas operation.[12,13] Otherwise, generation of overpressure is much simpler and cheaper compared to vacuum generation and recovery of the compression energy seems to be feasible especially for large industrial plants with high oxygen demand.[14]

According to that, different archetypes of MIEC membranes based on BSCF were prepared and characterized for oxygen permeation in vacuum operation mode.

Correspondence concerning this article should be addressed to M. Schulz at matthias.schulz@ikts.fraunhofer.de.

Table 1. Dimensions of the Prepared BSCF Membranes

Membrane Component	Outer Diameter [mm]	Inner Diameter (mm)	Membrane Thickness (mm)
Monolithic tube	15.5	12.6	1.45
Monolithic capillary	3.25	2.55	0.35
Asymmetric tube	14.5	11.6	–
7-Capillary module	3.25/15.5	2.55	0.35

Experimental

Sample preparation

All ceramic membrane components used were prepared using BSCF powder delivered by Treibacher Industrie AG, Austria. Pure single-phase cubic structure of the powder was proven by x-ray diffraction (XRD) measurements for all powder batches used.

Monolithic BSCF tubes and capillaries were prepared by plastic extrusion using a 50 and a 19 mm vacuum extruder made by ECT© and Brabender©. The dimensions of the sintered membranes are summarized in Table 1. The ceramic matter was prepared by aqueous plastification. Membrane tubes closed at one side were produced using a special extrusion die. The capillaries were produced using another simple ring-shaped extrusion die. Closing at one side was realized by squeezing the ''green'' ends of the capillaries using a modified crimping tool. All membranes were sintered at 1130°C for 2 h in air. Membrane tubes and capillaries with a total length up to 70 cm were obtained.

Tubular porous supports for asymmetric membranes closed at one side were prepared by plastic extrusion as described above using a mixture of 30% of a fine BSCF powder together with a coarse one. The open porosity of uncoated sintered supports measured by Hg intrusion amounted ~31 vol % with a pore diameter around 6 μm. A tortuosity of about 5 was determined by nitrogen permporosimetry at room-temperature for the uncoated support tubes.

The dense BSCF membrane layer was deposited by five different coating steps including dip coating, paste coating, and electrophoresis combined with intermediate sintering. The final surface of such an asymmetric membrane is depicted in Figure 1 (left) together with a picture of a cross fractured section (right). Despite the small pin holes visible in Figure 1 (left), leakages below 0.08 mL Standard Temperature and Pressure (STP)/(cm^2 min) were proven by the evaluation of the pressure rise after application of a constant vacuum inside the membrane tubes.

Capillary modules were built up using seven single capillaries, a locking plate closing one end of all capillaries and a plate realizing a connection to the supply tube for oxygen withdrawal. A module with a total length of 25 cm was prepared with capillaries 12.5 cm long. The locking and the connecting plate were produced by CNC machining of BSCF green discs prepared by uniaxial compaction. The green discs possess a diameter of 18 mm and a thickness of about 3 mm. The design of the plates is depicted in Figure 2 (left) together with the seven-capillary module built up and tested.

The discs were ground after sintering to achieve planar surfaces. The capillaries were joined with the plates in a first step by reactive air brazing (RAB)[15,16] at 980°C for 60 min. After that, a 12.5 cm long BSCF tube was joined to the lower side of the connecting plate by the same method. The whole capillary module is shown in Figure 2 (right). Leakage rate of the module was below the detection limit ($<2.7 \times 10^{-4}$ mbar · L/s) of the vacuum test rig.

Oxygen permeation experiments

Oxygen permeation experiments were performed in a vacuum driven dead-end mode. The connection to the vacuum system was realized using an adapted silicone rubber sealing. The standard length of the samples amounted to 25 cm with an active heated length of around 18 cm extending into the furnace. The vacuum pressure $p_l(1)$ was determined by a pressure sensor located at the nearest point behind the sealing to the membrane. Inner diameter of the vacuum piping was kept much higher than the inner diameter of the membrane components to prevent pressure drops inside the piping.

A remarkable pressure drop at the vacuum side was expected for single capillaries because of their small inner diameter. Therefore, a capillary with a length of 40 cm was also passed through the furnace and pressure sensors were located at both cold ends realizing a dead end at the top. The corresponding vacuum pressure at the dead end was abbreviated as $p_l(2)$. Accordingly, pressure drop inside the capillary was simply determined by the pressure difference of these two pressure sensors.

Oxygen permeation was characterized by heating all samples to a constant temperature between 600 and 850°C followed by a systematic variation of the vacuum pressure between 20 and 200 mbar using a pressure control valve. Ambient air was used as feed gas inside the open furnace purged by free convection. An enhanced purging with air driven by an electric fan has no effect to the oxygen permeation even at very high oxygen fluxes. Therefore, an influence

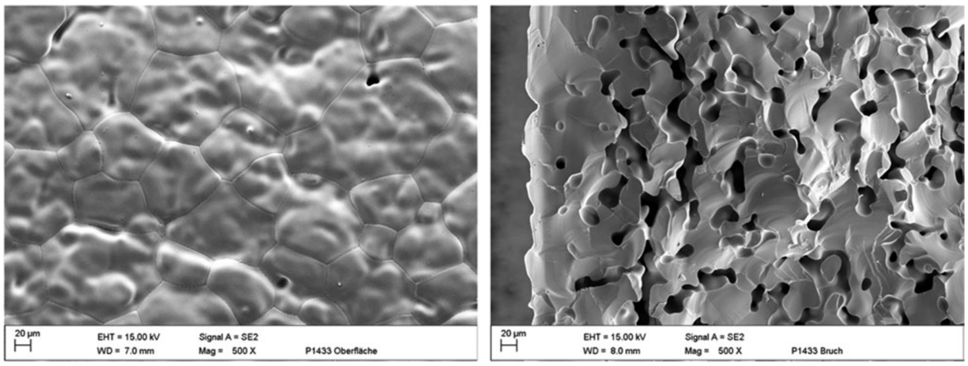

Figure 1. Scanning electron microscopy (SEM) images of a sintered asymmetric BSCF membrane tube, surface (left) and fracture face (right).

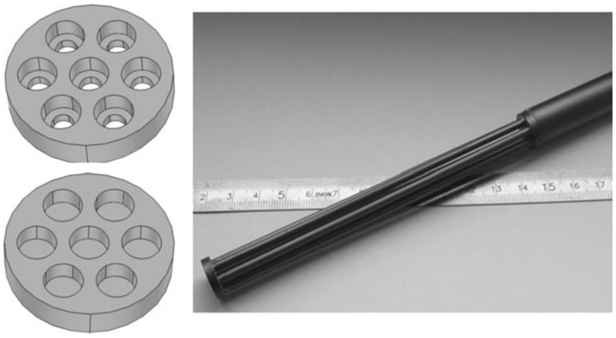

Figure 2. Design of the connecting plate (left above) and the closing plate (left below) used for BSCF capillary modules; BSCF capillary module (right).

by oxygen depletion at the feed side was excluded. Accordingly, the driving force for oxygen permeation was defined by the vacuum pressure inside the membrane sample $p_l(1)$ or $p_l(2)$ and the oxygen partial pressure of ambient air set to $p_h = 0.209$ bar. The scheme of the permeation test rig with a standard sample geometry and an extended sample length for pressure drop experiments is depicted in Figure 3.

The permeated oxygen was extracted using an oil-free vacuum pump ACP15 by Alcatel with a nominal suction speed of 15 m^3/h and a leakage rate below 5×10^{-7} mbar*L*s^{-1}. High oxygen fluxes Q_{O_2} were directly determined by the use of a mass flow meter calibrated to pure oxygen at standard conditions (1013.25 mbar, 273.15 K). Because of the high inaccuracy expected for small fluxes permeated oxygen was alternatively diluted by a well-defined nitrogen flux $Q_{N_2} = 250$ mL (STP)/min behind the vacuum pump. The oxygen content of the nitrogen was analyzed by two electrochemical zirconia sensors (ZIROX®, Germany) before and after the mixing point. In the case of nitrogen dilution, the flux of permeated oxygen was calculated according to Eq. 1,

$$Q_{O_2} = \frac{Q_{N_2}(p_{l,out}/p_{total} - p_{l,in}/p_{total})}{1 - p_{l,\,out}/p_{total}} \qquad (1)$$

where $p_{l,out}$ is the oxygen partial pressure of the nitrogen after mixing with the permeated oxygen in bar, $p_{l,in}$ is the oxygen partial pressure of the incoming nitrogen and p_{total} is the total pressure of the ambient air.

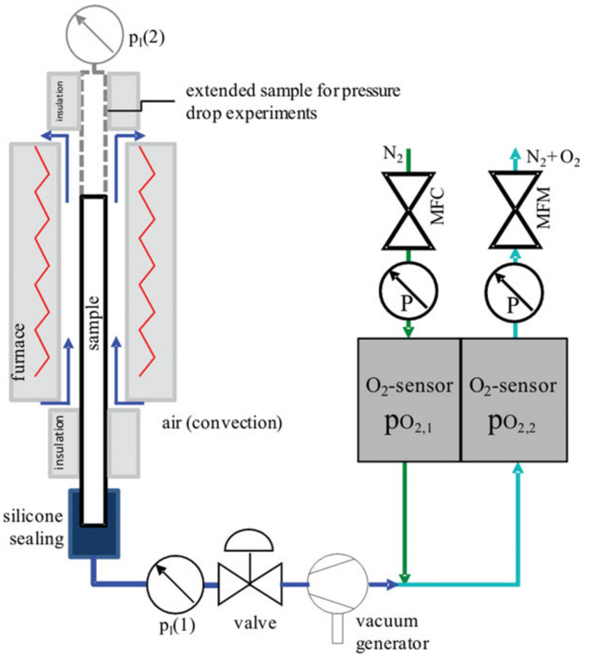

Figure 3. Schematic diagram of O_2 permeation test rig for measurements in vacuum operation mode.

[Color figure can be viewed in the online issue, which is available at wileyonlinelibrary.com.]

The operation conditions of permeation experiments were held constant to realize comparable results for all used membrane archetypes. Accordingly, all samples were built into the furnace at the same position and equal heating rates and dwell times were used. The characteristic sample temperature was determined using a 0.5 mm thick thermocouple placed inside the different membrane components at the same vertical position. Accordingly, it was assumed that the temperature distribution was comparable for all samples.

Because of the uncertain membrane area contributing to the oxygen flux density j_{O_2}, the total oxygen amount or oxygen flux was used as a primary result preferred for evaluation.

Results and Discussion

Monolithic BSCF membranes

Oxygen fluxes Q_{O_2} of monolithic tubular membranes depend on driving force are depicted in Figure 4 for different temperatures. Obviously, a clear linear relationship between O_2 flux and driving force was found for all temperatures with a high correlation of $R^2 > 0.99$. Accordingly, no deviation from Wagner behavior was detected according to our previous results.[11] As expected for the high wall thickness of 1.45 mm, the oxygen flux is restricted by the ionic transport and no hints for surface exchange limitations or further limitations were observed. This agrees with results published by Hong and Choi[17] and Kovalevsky et al.[18] discussing a surface limitation of BSCF membranes for a thickness below 1 mm.

Oxygen fluxes of single capillaries are depicted in Figure 5. In contrast to the thick-walled membrane tubes, a distinct

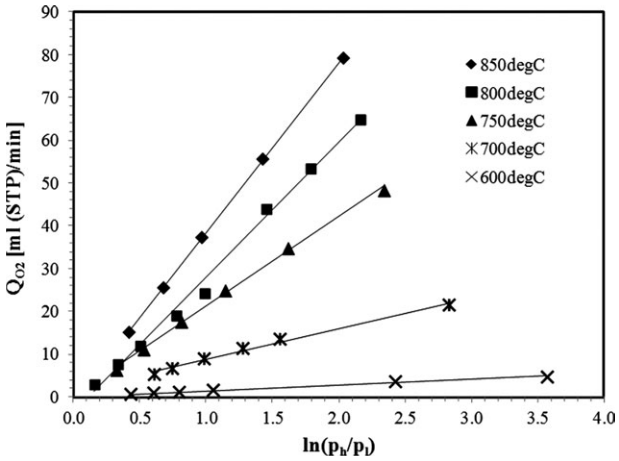

Figure 4. Oxygen flux through monolithic tubular BSCF membranes with a wall thickness of 1.45 mm at different temperatures in vacuum operation.

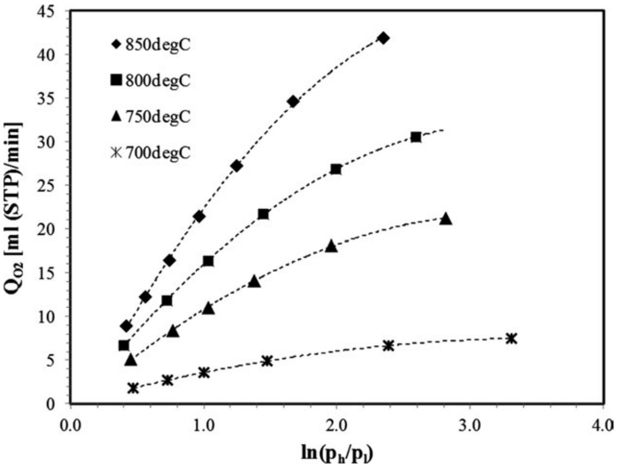

Figure 5. Oxygen flux through a BSCF capillary in vacuum operation mode at different temperatures, dashed lines for visual guidance.

negative deviation from the expected linear behavior according to Wagner was observed, especially at higher driving forces. This could be caused by surface limitations, especially by interactions between driving force and surface exchange as described by Kharton et al.[19] for materials based on strontium cobaltite. Similar results were also published by Kim et al.[20] An easier explanation is based on the pressure drop inside of capillary membranes already discussed by Yoon et al.[21] and Shao and Huang.[22] To identify the real cause, modified permeation experiments with longer capillaries were performed to determine the pressure drop along the capillaries. The experimental results were compared with multiphysics finite element simulations using the software COMSOL®.

The modified experimental set up for the determination of the pressure drop inside a long capillary is illustrated in Figure 3 by the gray dashed sample extension. The difference between both experimental pressures $p_l(1)$ and $p_l(2)$ corresponds to the total pressure drop along the long capillary. A maximal pressure drop of 17.1 mbar was observed at the lowest vacuum pressure of 20 mbar and a temperature of 850°C.

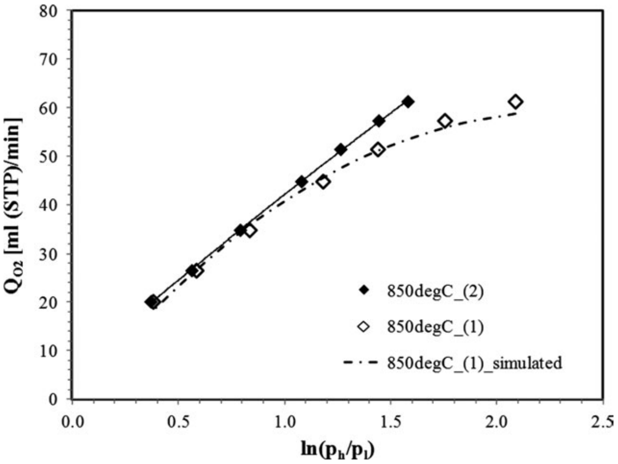

Figure 6. Oxygen flux of a 40-cm long BSCF capillary at 850°C plotted against the driving force calculated using the vacuum pressure *p*l(1) and *p*l(2); symbols for experimental results, solid line for linear regression, dashed line for simulations.

Figure 6 shows the oxygen flux of a long capillary with a length of 40 cm at 850°C depending on the driving force. Latter one was calculated alternatively using the vacuum pressure $p_l(1)$ at the entry and $p_l(2)$ at the dead end of the capillary. Obviously, the use of vacuum pressure at the dead end results in a reduced driving force and straightens the curve into a linear behavior. However, it has to be kept in mind that the temperature varies along the capillary from one cold end to the hot zone and to the other cold end again. Correspondingly, gas viscosity is much higher in the hot zone and pressure drop varies along the capillary depending on local temperature and on the absolute local vacuum pressure interacting with the local oxygen flux. Therefore, the calculation of the driving force using $p_l(2)$ is not entirely accurate. Nevertheless, the excellent linear relation between the oxygen flux and the driving force calculated using $p_l(2)$ indicates that the remaining error should be very low.

Multiphysics finite element calculations were performed to explain the experimental results for long and short capillaries. Thermophysical gas properties, the allocation of temperature along the capillary and a model for calculating the local oxygen flux[23] were taken into account. The simulated oxygen fluxes and pressure drops agree well with the experimental values. This is confirmed in Figure 6 by the simulated curve related to the uncorrected experimental values and by Figure 7 containing the calculated local vacuum pressure, the calculated local oxygen flux and the local experimental temperatures vs. the capillary length. As depicted in Figure 7, the experimental vacuum pressures at the open end of the capillary ($p_l(1) = 0.0361$ bar, 0 cm) and at the dead end ($p_l(2) = 0.043$ bar, 40 cm) agree well with the end points of the simulated vacuum pressure curve. Figure 7 also shows the calculated local oxygen fluxes j_{O_2} influenced significantly by local temperature and local vacuum pressure.

The simulation model validated for long capillaries was also used for the simulation of a short capillary with a length of 25 cm. Figure 8 shows the pressure drops calculated for vacuum pressures varying between 0.02 and 0.18 bar at the open capillary entry. Obviously, the pressure drop increases exponentially with decreasing vacuum pressure $p_l(1)$.

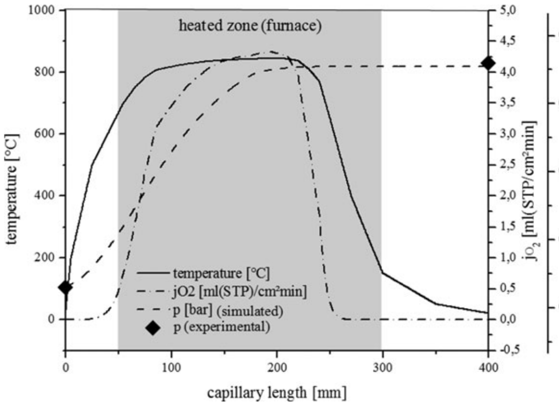

Figure 7. Simulated (curve) and experimental determined (symbols) vacuum-pressures as well as simulated oxygen flux and experimental determined temperatures along a long capillary (400 mm) at 850°C.

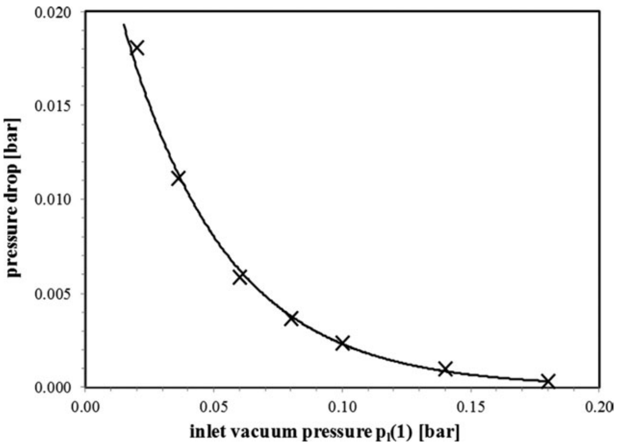

Figure 8. Simulated pressure drops inside a 25 cm long one end closed BSCF capillary at 850°C at various vacuum pressures *pl*(1), solid line for exponential regression.

All together, all deviations from a Wagner behavior observed for capillaries can be explained by pressure drops at the vacuum side. Therefore, a surface exchange limitation of the oxygen flux can be neglected for thin-walled capillaries at 850°C. This conclusion agrees well with results published by Buysse et al.[24] for BSCF capillaries with similar dimensions.

Capillary module

As mentioned earlier, seven BSCF capillaries with a length of 12.5 cm were bundled to a module using the RAB joining method. The oxygen flux of the module in vacuum operation is depicted in Figure 9 for several temperatures. The maximum oxygen flux of 175.5 mL(STP)/min was determined at 850°C at a vacuum pressure of $p_l(1) = 0.042$ bar. In contrast to measurements on single capillaries, no limitations of the oxygen flux at low-vacuum pressures entailed by high driving forces were observed. A high-correlation coefficient of $R^2 > 0.99$ was found for a linear regression proving an excellent agreement with a behavior according to Wagner.

Obviously, no significant pressure drop could have been present inside the capillary module down to a vacuum level of 0.04 bar. Numeric simulations revealed that the pressure drop for a single capillary amounts to nearly 10 mbar at these conditions but much lower values were obtained for the capillary module.

A maximum pressure drop of 2.7 mbar was calculated for the central capillary at 850°C and 0.042 bar. This is mainly caused by the introduced thermo couple with an outer diameter of 0.5 mm decreasing the free cross-section. The pressure drop inside the six outer capillaries surrounding the central one was calculated to 1.5 mbar only. Because of the same open cross-section of the single capillary and the capillaries bundled to a module, these serious differences seem to be unusual. Anyway, a detailed look at the flow velocities of the permeated oxygen revealed significant differences. Despite the oxygen flux much higher for the capillary bunch, the wide open cross-section of the oxygen withdrawal tube decreases the flow velocities there entailed by very low pressure drops. The maximum flow velocity at the outlet of the capillary module was calculated to 3.9 m/s. The flow velocity at the outlet of a single capillary amounted to 5.85 m/s at the same conditions. Accordingly, the overall pressure drop inside the capillary module is low compared to the expectations derived from the results of a single capillary.

Asymmetric tubular membranes

Oxygen permeation measurements on asymmetric tubular BSCF membranes revealed high oxygen fluxes of 142 mL(STP)/min at 850°C and a vacuum pressure $p_l(1)$ of 0.049 bar. Nevertheless, an increasing negative deviation of the oxygen flux from linearity was observed for decreasing vacuum pressure as depicted in Figure 10. Because of the wide open cross-section of the asymmetric membrane tubes, a limitation of oxygen flux caused by pressure drops inside the open space of the membrane tube was excluded.

Generally, the transport of oxygen within the porous support happens by gas diffusion (molecular and Knudsen) and by the viscous flow driven by pressure differences. Several authors[18,25] revealed a limitation of the oxygen flux caused by slow gas diffusion and concentration polarization[26–28] inside a porous support. The median pore diameter of the porous support around 6 μm pleads for Knudsen diffusion.

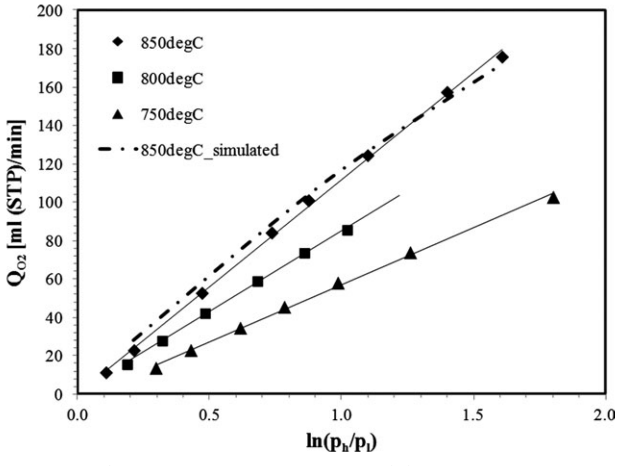

Figure 9. Oxygen flux through a BSCF capillary module in vacuum operation mode at different temperatures, solid lines for linear regression, dashed line for FE-simulations.

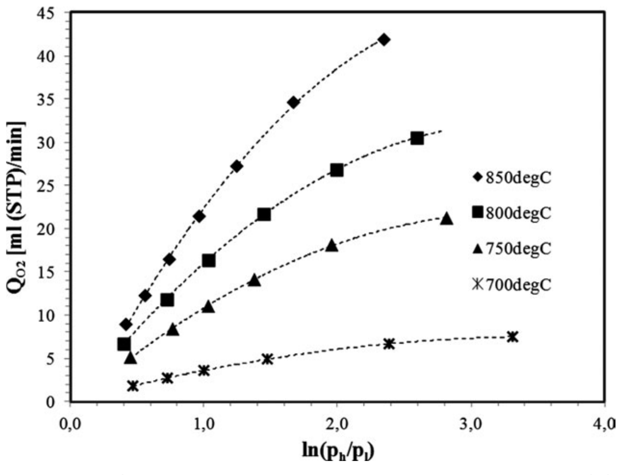

Figure 10. Oxygen flux through an asymmetric BSCF tube in vacuum operation mode at different temperatures, dashed lines for visual guidance.

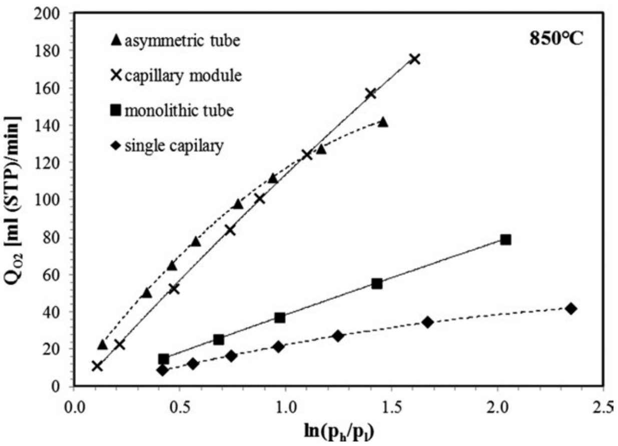

Figure 11. Comparison of the oxygen flux of various archetypes of BSCF membranes in vacuum operation mode at 850°C, solid lines for linear regression, dashed lines for visual guidance.

Besides, the main free path length of the oxygen molecules increases with decreasing vacuum pressure and Knudsen diffusion becomes more likely in the same way. Conversely, it can be assumed that the pressure drop across the porous support will increase with growing oxygen flux caused by decreasing vacuum pressures. Correspondingly, both transport mechanisms results in an increasing limitation of the oxygen flux with decreasing vacuum pressure.

Besides, a limitation of the oxygen flux by the surface exchange will be much more likely for the asymmetric membrane compared to the other components tested. Here the small wall thickness amounted to about 40 μm, which is comparable to the critical membrane thickness that could be expected for BSCF at 850 °C. Baumann et al.[26] and Etchegoyen et al.[29] propose the application of porous activation layers on top of the separation layer to accelerate the surface exchange and to enhance the oxygen permeation. Therefore, some attempts were made with coatings based on very fine BSCF powder, but no significant effect on the oxygen flux was observed.

Comparative assessment of various membrane archetypes

The oxygen flux of all tested membrane components are compared in Figure 11 for vacuum operation at 850°C. Obviously, the capillary module provides the highest oxygen flux with 175.5 mL(STP)/min at a low vacuum pressure of 0.042 bar measured at the membrane entry. The oxygen flux of the asymmetric membrane was comparable but increasing limitations occur at lower vacuum pressures or higher driving forces as described above. It has to be kept in mind that lower vacuum pressures are always accompanied by an increasing energy demand required for gas compression. Therefore, very low-vacuum pressures are not meaningful for an energy efficient separation process but could be interesting to control an industrial process and to compensate peak loads. Nevertheless, the asymmetric membrane demonstrates slight advantages compared to the capillary module for moderate vacuum pressures above 0.07 bar.

Table 2 summarizes the oxygen fluxes at 850°C and a moderate vacuum pressure of 0.1 bar as well as the theoretic nominal active membrane area A_{nom} for all membrane archetypes.

The nominal active membrane area was estimated by the division of the oxygen amount produced by the monolithic tube Q_{O_2} regarding to the oxygen flux $j_{O_2,\text{ref}}$ of tubular BSCF membranes used as a reference according to Eq. 2.

$$A_{\text{nom}} = \frac{Q_{O_2}}{j_{O_2,\text{ref}}} \tag{2}$$

Tubular reference samples are based on BSCF membrane tube pieces with a length of 5 cm joined to a steel tube by RAB. The membrane thickness and diameter were comparable to that one of the monolithic tube used in this work. Characterization was realized by vacuum permeation experiments using the same test rig. Because of the short sample length, isothermal and isobaric conditions were assumed and a well-defined oxygen flux density $j_{O_2,\text{ref}}$ was obtained.[30]

Using the results obtained for the reference samples, an unambiguous assignment of the oxygen flux to the membrane area was possible. For example, the monolithic membrane tube delivers about 26 mL (STP)/min oxygen at a nominal temperature of 850°C and an inlet vacuum pressure of 0.1 bar as described earlier. Naturally, this is accompanied by a variation of temperature, vacuum pressure, and oxygen flux density along the membrane axis. The corresponding oxygen flux density of the reference sample at isothermal and isobar conditions (850°C, 0.1 bar) was determined to 0.55 mL (STP)/(cm^2 min). Accordingly, the membrane area required to generate the same total oxygen flux of 26 mL (STP)/min at isothermal and isobar conditions results in a nominal membrane area of 45.8 cm^2. Using this value, a corresponding nominal membrane length contributing to the total oxygen flux can be easily determined using the diameter of the membrane tube. This characteristic active membrane length of 9.4 cm should be constant for all membrane types characterized with this test rig if the temperature profile is comparable. Accordingly, the nominal membrane area A_{nom} of other membrane archetypes was calculated using this characteristic active membrane length and the geometric dimensions of the membrane component. An averaged value derived from inner and outer diameter was usually used for that. In the case of asymmetric membranes, the outer diameter was used because of the application of the separation layer at the outer surface.

The oxygen flux density j_{O_2} of the various membrane components investigated was then calculated according Eq. 3.

$$j_{O_2} = \frac{Q_{O_2}}{A_{\text{nom}}} \tag{3}$$

Thus, the nominal active membrane area A_{nom} was used as an auxiliary variable to realize a rough and simplified comparison of the different membrane types regarding the oxygen flux density.

Table 2. Theoretical Active Membrane Area A_{nom}, Experimental Determined Oxygen Flux Q_{O_2} and Oxygen Flux Density j_{O_2} for Different Membrane Types at 850°C and 0.1 bar

Membrane type	Nominal active membrane area A_{nom} (cm^2)*	Q_{O_2} [mL (STP)/min]	j_{O_2} [mL (STP) /(cm^2 min)]†
Single capillary	8.6	16	1.87
Monolithic tube	41.5	25	0.60
Capillary module	59.9	84	1.40
Asymmetric tube	42.8	98	2.29

*Calculated from Eq. 2
†Calculated from Eq. 3

As expected, the highest active membrane area of 59.9 cm^2 was obtained for the capillary module, but the monolithic and asymmetric tube maintained after all a membrane area around 65% thereof. This effect increases the oxygen flux of the module slightly, but the main effect for flux enhancement is caused by the lower wall thickness. For the same reason, the oxygen flux of the asymmetric membrane with a further decreased wall thickness exceeded that one of the module despite its lower membrane area.

The nominal active membrane area of 59.9 cm^2 for the capillary module consisting of seven single capillaries corresponds to a nominal active length of 9.4 cm. A single capillary delivers 16 mL (STP)/min and the seven-fold flux value (112 mL (STP)/min) should be expected for the module consisting of seven capillaries with 12.5 cm length. That means the connector plate of the module is located outside the hot zone and only the hot part of the capillaries contributes to the oxygen flux. However, the capillary module delivers 84 mL (STP)/min only corresponding to a total flux of 75% related to the expectations. This mismatch might be explained by the contributions of membrane regions relatively cold related to the nominal temperature of the hot zone. Figure 7 shows that the real hot zone is much longer than the nominal active membrane length, but the real temperature is much lower than 850°C for most part of the real hot zone. Correspondingly, the membrane length contributing to the whole oxygen flux is much longer than 9.4 cm. In the case of a single capillary or another membrane component with homogeneous design, the whole membrane contributes to the oxygen flux corresponding to the real temperature distribution. In contrast to that, the capillary module generates oxygen mainly along the length of 12.5 cm of the individual capillaries, but the contribution of the thick-walled supply tube should be very low. In this context, it has to be kept in mind that the constant active length of 9.4 cm used for recalculation of the nominal membrane area is only a mathematical tool without physical meaning. In reality, membrane area outside this length will also contribute to the total oxygen flux especially if the wall thickness is low.

Conclusions

Various archetypes of BSCF membranes were characterized regarding the oxygen flux in vacuum operation mode. The normalization to the membrane area revealed the highest oxygen flux density for the asymmetric membrane with 2.4 mL (STP)/(cm^2 min) at moderate driving forces. Correspondingly, asymmetric membranes should be used at low driving forces according to the increasing flux limitations with decreasing vacuum pressures. The capillary module seems to be predestined for vacuum pressures below 70 mbar because of the lack of flux limitations at these conditions. Nevertheless, pressure drops has to be take into account for long modules and small inner diameters of the capillaries used. Single capillaries need much lower installation space than monolithic thick-walled membrane tubes. Together with the higher oxygen flux density, small oxygen generators or devices with integrated oxygen supply could be realized much easier. Therefore, single capillaries could be used for integration of oxygen separation membranes into small devices with limited installation space or reaction volume. However, it has to be kept in mind that the pressure drop of single capillaries is significantly higher compared to capillary modules built up on an oxygen withdrawal tube with sufficient inner diameter.

The oxygen flux through monolithic tubes and capillaries can be described according to Wagner. All deviations observed were caused by pressure drops at the permeate side, especially, at low-vacuum level and small cross-sections of the membrane components. Therefore, a limitation of the oxygen flux by surface exchange can be excluded also for thin capillaries with a membrane thickness of 0.35 mm only. Flux deviations observed for asymmetric membranes could be caused not only by surface exchange limitations but also by pressure drops inside the porous support. A doubtless clarification seems to be not possible without further investigations.

The enhancement of the oxygen flux by advanced membrane components improves the competitiveness of the membrane separation process because of the smaller size of membrane reactors entailed by decreasing heat loss and energy demand. However, this advantage rivals directly with the costs for the production of advanced membrane components. According to that, technology has to be developed for fast and cheap production of complex membrane archetypes. Looking onto the five-fold coating process for the production of asymmetric membranes, this is a very ambitious objective.

Acknowledgments

Financial support from the Helmholtz Association of German Research Centres (Initiative and Networking Fund) through the Helmholtz Alliance MEM-BRAIN, contract HA-104, is gratefully acknowledged as well as the financial support of the Federal Ministry of Economy and Infrastructure under grant number MF090096.

Literature Cited

1. Bredesen R, Sogge J. *A technical and economic assessment of membrane reactors for hydrogen and syngas production*. In: *Seminar on the Ecological Applications of Innovative Membrane Technology in the Chemical Industry*, Cetraro, Italy, 1996.
2. Vente JF, Haije WG, IJpelaan R, Rusting FT. On the full-scale module design of an air separation unit using mixed ionic electronic conducting membranes. *J Membr Sci*. 2006;278:66–71.
3. Kriegel R, Schulz M, Ritter K, Kiesel L, Pippardt U, Stahn M. *Advanced membrane design for oxygen separation*. In: *Proceedings of the 2nd International Conference on Energy Process Engineering (ICEPE 2011): Efficient Carbon Capture for Coal Power Plants*, 2011:114–117.
4. Shao Z, Yang W, Cong Y, Dong H, Tong J, Xiong G. Investigation of the permeation behavior and stability of a $Ba_{0.5}Sr_{0.5}Co_{0.8}Fe_{0.2}O_{3-\delta}$ oxygen membrane. *J Membr Sci*. 2000;172:177–188.
5. Haihui W, Weishen Y, Cristina T, Caro J. Oxygen diffusion in oxide crystals—tracing new routes to identify the rate limiting step of oxygen permeation through perovskite membranes. *Diffus Fundam*. 2005;2:46.1–46.15.
6. Lu H, Tong J, Cong Y, Yang W. Partial oxidation of methane in $Ba_{0.5}Sr_{0.5}Co_{0.8}Fe_{0.2}O_{3-\delta}$ membrane reactor at high pressures: catalysis in membrane reactors catalysis in membrane reactors proceedings of the 6th international conference on catalysis in membrane reactors. *Catal Today*. 2005;104:154–159.
7. Vente JF, Haije WG, Rak ZS. Performance of functional perovskite membranes for oxygen production. *J Membr Sci*. 2006;276:178–184.
8. Vente J, McIntosh S, Haije W, Bouwmeester H. Properties and performance of $Ba_xSr_{1-x}Co_{0.8}Fe_{0.2}O_{3-\delta}$ materials for oxygen transport membranes. *J Solid State Electrochem*. 2006;10:581–588.
9. Svarcova S, Wiik K, Tolchard J, Bouwmeester HJM, Grande T. Structural instability of cubic perovskite $Ba_xSr_{1-x}Co_{1-y}Fe_yO_{3-\delta}$. *Solid State Ionics*. 2008;178:1787–1791.
10. Arnold M, Gesing TM, Martynczuk J, Feldhoff A. Correlation of the formation and the decomposition process of the BSCF perovskite at intermediate temperatures. *Chem Mater*. 2008;20:5851–5858.
11. Kriegel R. *Einsatz keramischer BSCF-Membranen in einem transportablen Sauerstoff-Erzeuger*. In: Deutsche Keramische Gesellschaft, editor. *Handbuch Technische Keramische Werkstoffe [Loseblattwerk]*: HvB-Verlag Ellerau, Ellerau, Germany, 2010; *Chapter 8.10.1.1, S*. 1–46.

12. Tan X, Li K. Oxygen production using dense ceramic hollow fiber membrane modules with different operating modes. *AIChE J*. 2007;53:838–845.
13. Kriegel R, Burckhard W, Voigt I, Schulz M, Sommer E. *Benefits of the vacuum process for oxygen production from air using* $Ba_xSr_{1-x}Co_{1-y}Fe_yO_{3-\delta}$ *membranes*. In: *Proceedings of the 10th International Conference on Inorganic Membranes (ICIM10)*, Tokyo, Japan, 2008.
14. Engels S, Beggel F, Modigell M, Stadler H. Simulation of a membrane unit for oxyfuel power plants under consideration of realistic BSCF membrane properties: Membranes and CO_2 Separation. *J Membr Sci*. 2010;359:93–101.
15. Weil KS, Hardy JS, Rice JP, Kim JY. Brazing as a means of sealing ceramic membranes for use in advanced coal gasification processes: Special Issue: The 21st Annual International Pittsburgh Coal Conference. *Fuel*. 2006;85:156–162.
16. Erskine K, Meier A, Pilgrim S. Brazing perovskite ceramics with silver/copper oxide braze alloys. *J Mater Sci*. 2002;37:1705–1709.
17. Hong WK, Choi GM. Oxygen permeation of BSCF membrane with varying thickness and surface coating. *J Membr Sci*. 2010;346: 353–360.
18. Kovalevsky AV, Yaremchenko AA, Kolotygin VA, et al. Oxygen permeability and stability of asymmetric multilayer $Ba_{0.5}Sr_{0.5}Co_{0.8}Fe_{0.2}O_{3-\delta}$ ceramic membranes: Proceedings of the 17th International Conference on Solid State Ionics. *Solid State Ionics*. 2011;192:677–681.
19. Kharton VV, Kovalevsky AV, Yaremchenko AA, Figueiredo, FM, Naumovich, EN, Shaulo, AL, Marques, FMB. Surface modification of $La_{0.3}Sr_{0.7}CoO_{3-\delta}$ ceramic membranes. *J Membr Sci*. 2002;195:277–287.
20. Kim S, Yang YL, Jacobson AJ, Abeles B. Diffusion and surface exchange coefficients in mixed ionic electronic conducting oxides from the pressure dependence of oxygen permeation. *Solid State Ionics*. 1998;106:189–195.
21. Yoon S, Lee S, Yeom I. Experimental verification of pressure drop models in hollow fiber membrane. *J Membr Sci*. 2008;310:7–12.
22. Shao P, Huang RYM. An analytical approach to the gas pressure drop in hollow fiber membranes. *J Membr Sci*. 2006;271:69–76.
23. Schulz M. *Modeling of oxygen flux and stress distribution for* $Ba_{0.5}Sr_{0.5}Co_{0.8}Fe_{0.2}O_{3-\delta}$ *membranes at application conditions*, 2008, Tokyo.
24. Buysse C, Kovalevsky A, Snijkers F, et al. Development, performance and stability of sulfur-free, macrovoid-free BSCF capillaries for high temperature oxygen separation from air. *J Membr Sci*. 2011;372:239–248.
25. Kawahara A, Takahashi Y, Hirano Y, Hirano M, Ishihara T. Importance of pore structure control in porous substrate for high oxygen penetration in $La_{0.6}Sr_{0.4}Ti_{0.3}Fe_{0.7}O_3$ thin film for CH_4 partial oxidation. *Solid State Ionics*. 2011;190:53–59.
26. Baumann S, Serra JM, Lobera MP, Escolástico S, Schulze-Küppers F, Meulenberg WA. Ultrahigh oxygen permeation flux through supported $Ba_{0.5}Sr_{0.5}Co_{0.8}Fe_{0.2}O_{3-\delta}$ membranes. *J Membr Sci*. 2011;377: 198–205.
27. Lobera MP, Serra JM, Foghmoes SP, Soegaard M, Kaiser A. On the use of supported ceria membranes for oxyfuel process/syngas production. *J Membr Sci*. 2011;385–386:154–161.
28. Feng X, Ivory J, Rajan VSV. Air separation by integrally asymmetric hollow-fiber membranes. *AIChE J*. 1999;45:2142–2152.
29. Etchegoyen G, Chartier T, Del-Gallo P. An architectural approach to the oxygen permeability of a $La_{0.6}Sr_{0.4}Fe_{0.9}Ga_{0.1}O_{3-\delta}$ perovskite membrane. *J Eur Ceram Soc*. 2006;26:2807–2815.
30. Schulz M. *FEM-Simulation der Sauerstoffpermeation durch MIEC Membranen im Vakuumbetrieb und Vergleich mit experimentellen Daten*; March 23, 2010; Deutsche Keramische Gesellschaft conference. Hermsdorf.

Manuscript received Mar. 7, 2012, and revision received Apr. 24, 2012.